ARITHMETIC METHODS
IN MATHEMATICAL PHYSICS AND BIOLOGY
BANACH CENTER PUBLICATIONS, VOLUME 109
INSTITUTE OF MATHEMATICS
POLISH ACADEMY OF SCIENCES
WARSZAWA 2016

MULTIFRACTAL FORMALISM IN IMAGE AND TIME SERIES ANALYSIS

AUDREY L. KARPERIEN
Centre for Research in Complex Systems, Charles Sturt University
Albury, Australia
E-mail: akarperien@yahoo.com

HERBERT F. JELINEK
School of Community Health & Centre for Research in Complex Systems
Charles Sturt University, Albury, Australia
E-mail: hjelinek@csu.edu.au

HELMUT AHAMMER
Institute of Biophysics, Centre for Physiological Medicine, Medical University of Graz
Graz, Austria
E-mail: helmut.ahammer@medunigraz.at

Abstract. Multifractal analysis explores patterns to discover within them characteristic sets of multiple fractal dimensions. Using computer software, patterns are resolved over decreasing scales and examined under various distorting lenses to make multifractal spectra that can sometimes tell much about the state of a system, including physiological systems. Here we review some key tenets of the multifractal formalism using box-counting as the basis for software-based multifractal analysis, and discuss some applications to cell morphology, retinal pathology, cancer, and heart rate variability.

1. Introduction. Where are fractals found? In this age of booming digital information and convenient computer capacity, fractal analysis is burgeoning across many disciplines. Indeed, one is hard-pressed to find an area in which investigators have not at least started to view phenomena through the modern lenses of fractal analysis. Fractal

2010 *Mathematics Subject Classification*: 28A80.
Key words and phrases: multifractal, microglia, fractal analysis, box-counting, retinopathy, heart rate variability, cardiac autonomic neuropathy, cervical intraepithelial neoplasia, ImageJ, image analysis.
The paper is in final form and no version of it will be published elsewhere.

analysts have found meaning in and in many cases practical uses for the fractal features lurking in an incredible variety of physical as well as social phenomena including

- Galactic star distributions [65] and Saturn's rings [53]
- River flows [17] and soil structure [72]
- Population distributions and urban expansion [6, 10]
- Road and building materials [87]
- Dendritic branching patterns, vascular networks, lung bronchioli [33, 74]
- Brain structure and function [18, 21, 24]
- Pathology such as cancer [43] and diabetic retinopathy [30, 31, 32, 48, 61, 63]
- Health care, clinical practice, and pharmacy [30, 69, 73, 79]
- Ion channel opening and closing times [8]
- Time series analysis (e.g., gait, EMG, ECG, EEG) [19, 77, 78]
- Codes (e.g., DNA) [62]
- Classification of images [38].

1.1. Multifractal analysis of 1D and 2D images in biology and medicine. This chapter distills from the variety of types and topics in fractal analysis a limited look at a set of methods called *multifractal analysis*. We review essential mathematical techniques and discuss the multifractal formalism with respect to applications in biology and medicine. The particular topics we look at in biology and medicine are microglial cell analysis, diabetic retinopathy, cancer, and heart rate variability.

In essence, all fractal analyses examine the scaling inherent in a pattern or dataset and assign to that scaling a "rule" or number known as a fractal dimension (D_F), which is a statistical index of complexity having no units [27, 56]. As is typical in biology, the morphologies and physiological events we examine here are generally cascading, recursive, thresholded phenomena having patterns characterized by not one but multiple such scaling rules, i.e., they can be shown to be multifractal [56, 74].

1.2. Estimating the D_F. As grounding for understanding *multi*-fractal analysis, one should first be familiar with *mono*-fractal analysis and the way the so-called monofractal dimension is estimated. This is important not only for understanding the multifractal formalism, but also because mono- and multi-fractal analysis methods complement each other in certain ways, as will be discussed later here. The basic method depends on the essential concept in fractal theory of patterns that repeat themselves regardless of the scale at which they are observed, i.e., *self-similarity* [33, 58]. Such scaling can be measured by observing a phenomenon at a starting resolution of nominally 1 (i.e., it is viewed as one whole part, $N_0 = 1$), then repeatedly scaling the observation by some factor, ϵ, some number of times, k, and counting each resulting number of parts (N_k). To measure scaling in a simple line-drawing, this would generate a series using as an example, $\epsilon = \frac{1}{3}$, consisting of $N_0 = 1$, $N_1 = 1 \times (\frac{1}{3})^{-1} = 3$, $N_2 = 3 \times (\frac{1}{3})^{-1} = 9$, $N_3 = 9 \times (\frac{1}{3})^{-1} = 27$, and so on. That is, it is described by the general sequence

$$N_k = N_{k-1}\epsilon^{-1}. \tag{1}$$

Using $N_0 = 1$ gives the base scaling rule for a simple line-drawing:

$$N_1 = \epsilon^{-1}. \tag{2}$$

The negative of the exponent, the 1, on ϵ in Equation (2), quantifies the familiar, easily perceived unity between the number of new parts observed and the reduction factor used for measuring the scaling in a simple line. Despite the obviousness of this particular case, the process outlined above is not trivial—the value of the exponent is not always apparent, such as for a pattern that scales into $N = 4$ new parts when $\epsilon = \frac{1}{3}$ (see Figure 1, which shows a fractal von Koch Curve scaling in this manner). For that case, the sequence is $N_1 = 1 \times (\frac{1}{3})^{-D_F} = 4$, $N_2 = 4 \times (\frac{1}{3})^{-D_F} = 16$, $N_3 = 16 \times (\frac{1}{3})^{-D_F} = 64$, and so on. By substituting in the known values for any k and $k-1$, the D_F for the von Koch Curve can be found, as is shown in the example below using $k = 2$:

$$N_2 = N_1 \times \left(\frac{1}{3}\right)^{-D_F}$$

$$16 = 4 \times 3^{D_F} \implies 4 = 3^{D_F} \implies D_F = \frac{\ln 4}{\ln 3} \approxeq 1.2619.$$

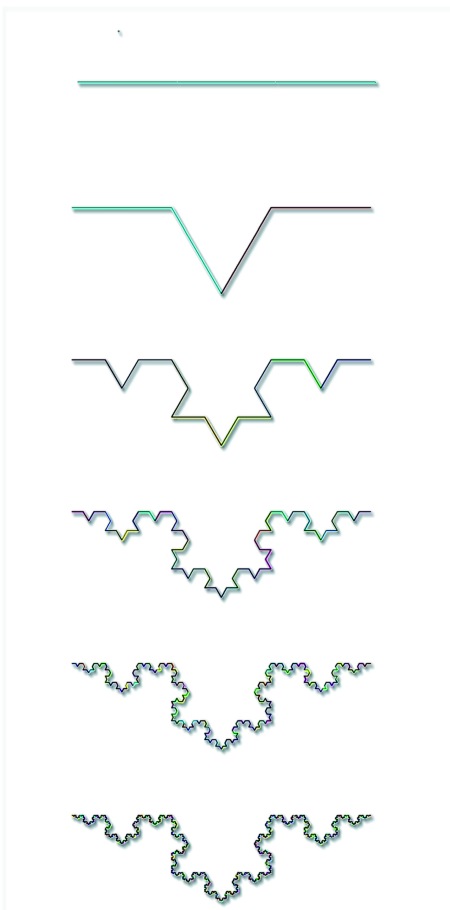

Fig. 1. *Iterating the pattern of a classic fractal von Koch Curve.* The figure shows how the curve can be constructed graphically. The basic procedure is to divide a line into 4 new parts each $\frac{1}{3}$ the size of the original, then repeatedly divide each new part in the same way as illustrated in the figure. Thus, the drawings, in sequence, would theoretically have $N = 1, 4, 16, 64$, 256, and 1024 parts respectively.

Note that the figure illustrates *limited self-similarity.* By closely inspecting or zooming in, especially on the bottom 2 iterations, one can see that the represented pattern repeats itself at each scaling but at the same time each level stops as straight segments of finite length. In contrast, the actual scaling in a real fractal von Koch Curve, or any *strictly self-similar* fractal pattern, repeats infinitely such that regardless of the scale at which it is inspected, the same pattern is found at a closer level of inspection, the pattern never resolving into linear segments with finite lengths.

Generated using the freeware Fractal Generator plugin for ImageJ http://imagej.nih.gov/ij/plugins/fractal-generator.html

This example highlights the general equation relating N_k and ϵ (Equation (3)) which is solved for the D_F in Equation (4):

$$N_k = \epsilon^{-kD_F}. \tag{3}$$

In general, for $k > 0$, the D_F can be calculated according to Equation (4), or, for the case that the base scaling is known, Equation (5):

$$D_F = -\frac{\ln N_k}{\ln \epsilon^k} = \frac{\ln N_k}{\ln \epsilon^{-k}}\,, \tag{4}$$

$$D_F = -\frac{\ln N}{\ln \epsilon} = \frac{lnN}{\ln \epsilon^{-1}}\,. \tag{5}$$

1.3. Box-counting. In the more practical world of biological research, the number of new parts a pattern scales into is usually not readily observable. Fortunately, there are many ways to extract from a pattern information required to use the general relationship in Equation (5). The method we discuss here, one often used for finding D_Fs for biological phenomena, is an elegant fractal analysis technique known as *box-counting,* which generates a type of D_F called the box-counting dimension (D_B). We discuss the method from the basis of binary images, meaning digital images showing patterns extracted from original images and converted into a form where there are only two choices for a pixel's state: background or non-background [38, 50, 57].

As its name suggests, this method finds scaling relationships in patterns by inspecting them using a box shape. The method is usually applied using dedicated fractal analysis software, which can generally be obtained as freeware for biologists (e.g., the downloadable FracLac for ImageJ [45, 67] or the online FracTop [13], both created and maintained by our lab).

To summarize, the general approach is to make a starting observation of a pattern by surrounding it with a box (i.e., $N_0 = 1$), then to continue making observations using smaller and smaller boxes scaled by ϵ at each iteration, k. The number of boxes that contain non-background pixels is considered as a proxy for N_k. The basic procedure is illustrated in Figure 2.

In practice, this method of making up the sequence N_k does not always yield a strictly consistent relationship between N and ϵ. The methods of fractal analysis introduce their own practical methodological issues. In addition to the grid position issue noted in Figure 2, there are various other issues that are beyond the scope of this discussion but are generally corrected for in dedicated box-counting software (e.g., adjustments have to be made to the maximum and minimum box sizes to yield valid results) (see [46]). One issue that should be discussed is how this works when the scaling factor is not usually known ahead of time, but a suitable starting factor has to be assumed in order to scale the boxes. The answer lies in the relationship between N_k and ϵ in many phenomena and in methods of determining D_Fs being statistical. Thus, the D_F is often estimated from the limit:

$$D_F = \lim_{\epsilon^{-k}\to 0}\Big[\frac{\ln N_k}{\ln \epsilon^{-k}}\Big]. \tag{6}$$

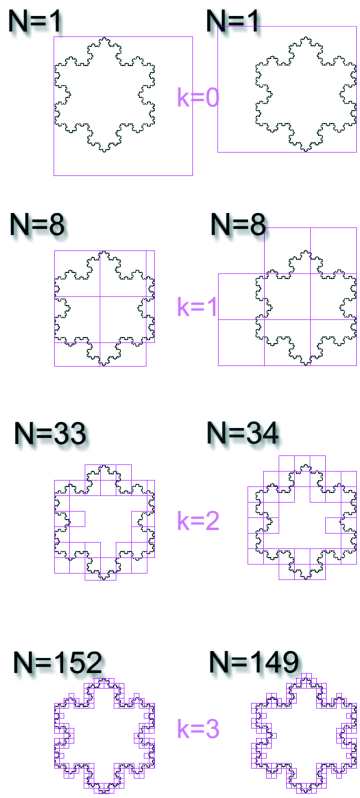

Fig. 2. *Box-counting.* The figure illustrates the basic algorithm used for automated computer-based box-counting using decreasing box sizes. The columns are for the same image, a von Koch Flake based on the von Koch Curve of Figure 1. Each column shows N_k, the number of boxes that contained any foreground pixels at each box size, B_k. The same 4 box sizes, successively scaled by $\epsilon = \frac{1}{3}$, were used for both columns.

Differences between the $k = 2$ counts and between the $k = 3$ counts reflect differences in where the boxes were placed. This illustrates the general point that if a pattern covers a rectangular rather than square area, there is no clearly optimal orientation at which to lay the first square box. Thus, box orientation affects N_k and the number of pixels per box at any ϵ. One way to address this limitation of box-counting is to use software that provides the mean or the minimum cover D_B over several orientations (e.g., FracLac for ImageJ [45, 67]).

Grid drawings generated using FracLac for ImageJ [45] and von Koch Flakes generated using the Fractal Generator plugin for ImageJ from http://imagej.nih.gov/ij/plugins/fractal-generator.html

1.3.1. *Regression lines and scaling series.* In box-counting, the limit is formally calculated as the slope of the log vs. log linear regression line for the data series. This makes it possible to use, instead of a known ϵ, virtually any series of decreasing box size (B), and to process the resulting data to find the most appropriate scaling. As a result, in box-counting implemented to do this, k for a series becomes merely an index in the list of B_k, rather than an actual indicator of the number of times scaled. Software designed for biologists, such as FracLac for ImageJ [46] generally includes mechanisms for controlling the scaling or actual values used to define each series of B and ensuring the resulting data are properly filtered to arrive at a consistent and meaningful scaling value. The D_B, accordingly, is generally calculated as the slope of the log vs. log regression line based on the series B_k rather than ϵ_k, as in Equation (7) [38, 45, 56, 75]

$$D_B = -\lim_{\mathrm{B}_k \to 0} \left[\frac{\ln N_k}{\ln \mathrm{B}_k} \right]. \tag{7}$$

2. Multi- vs. mono-fractal analysis. As was mentioned earlier here, multifractal analysis explores patterns to discover not just one global D_F describing a beautiful scaling relationship that preserves detail at all levels of resolution, but multiple such scaling rules. It looks at patterns by resolving them into smaller and smaller units, and exploring how

they behave when distorted by further applying various lenses (see Figure 3). We used two such lenses, the *generalized dimension* and the $f_{(\alpha)}$ spectrum.

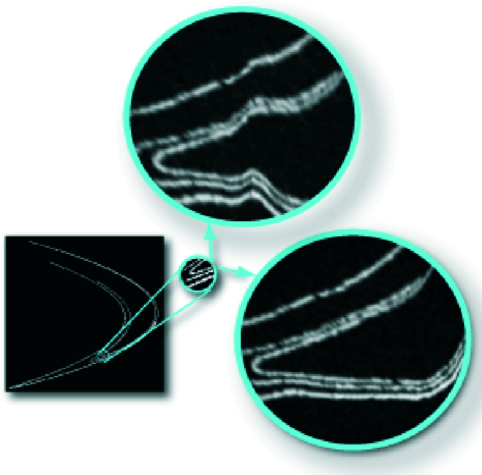

Fig. 3. *Conceptualizing multifractal analysis.* Multifractal analysis looks at how the mass of a pattern behaves when resolved into a series of successively scaled pieces and distorted. The picture illustrates a typical multifractal pattern known as a Henon Map, with a region amplified and distorted in two ways to conceptually represent localized distortions created by applying arbitrary exponents to the mass distribution during multifractal analysis.

Image author A. Karperien; WikimediaCommons. Henon Map generated using Fractal Growth Models plugin at http://imagej.nih.gov/ij/plugins/fgm/index.html for ImageJ.

Whereas the data for multifractal analysis can be gathered in the same way as was described in the previous section for standard *box-counting*, the type of information gathered is different. Instead of using N_k, i.e., the number of boxes for B_k that had non-background pixels in them, the method uses the number of pixels or *mass* (m) per individual box (i) at a particular size, B_k. Accordingly, this mass-related approach has for each B_k a distribution of $m_{(i,k)}$ that has a total number of members $= N_k$.

Similar to the general relationship between N_k and ϵ in Equation (3), for typical monofractals the probability $(P_{(i,k)})$ of a mass of pixels appearing in the i-th box varies as box size or scale to a constant exponent, which can be calculated similarly to the D_B, as the mass dimension (D_M):

$$P_{(i,k)} \approx \mathrm{B}_k^{-D_M} \therefore -D_M = \frac{\ln P_{(i,k)}}{\ln \mathrm{B}_k}\,. \tag{8}$$

Multifractals, however, are not homogeneous. $P_{(i,k)}$ changes according to an exponent, α_i, that varies over the fractal, as in the following equation [17, 22, 40]:

$$P_{(i,k)} \approx \mathrm{B}_k^{-\alpha_i} \therefore -\alpha_i \approx \frac{\ln P_{(i,k)}}{\ln \mathrm{B}_k}\,. \tag{9}$$

The exponent α_i is said to be the "singularity strength" or scaling in the i-th region. There is a set of boxes, N_{α_i}, that will have singularity strengths around this α_i and its fractal dimension is the function $f_{(\alpha_i)}$. In other words, N_{α_i} scales as $\mathrm{B}_k^{f_{(\alpha_i)}}$. Thus, multifractals are considered heterogeneous, and typically analyzed in terms of sets of dimensions that are used to generate spectra describing the scaling [12, 64].

2.1. The generalized dimension. One set of dimensions used extensively in multifractal analysis is the set of *generalized dimensions* or D_Q, where Q is an arbitrary set of exponents used to distort and examine the mass distribution. For digital images, D_Q describes how the distribution of pixels behaves when an image is resolved into a series

of k scalings and the distribution is distorted and re-examined to emphasize differences over the pattern.

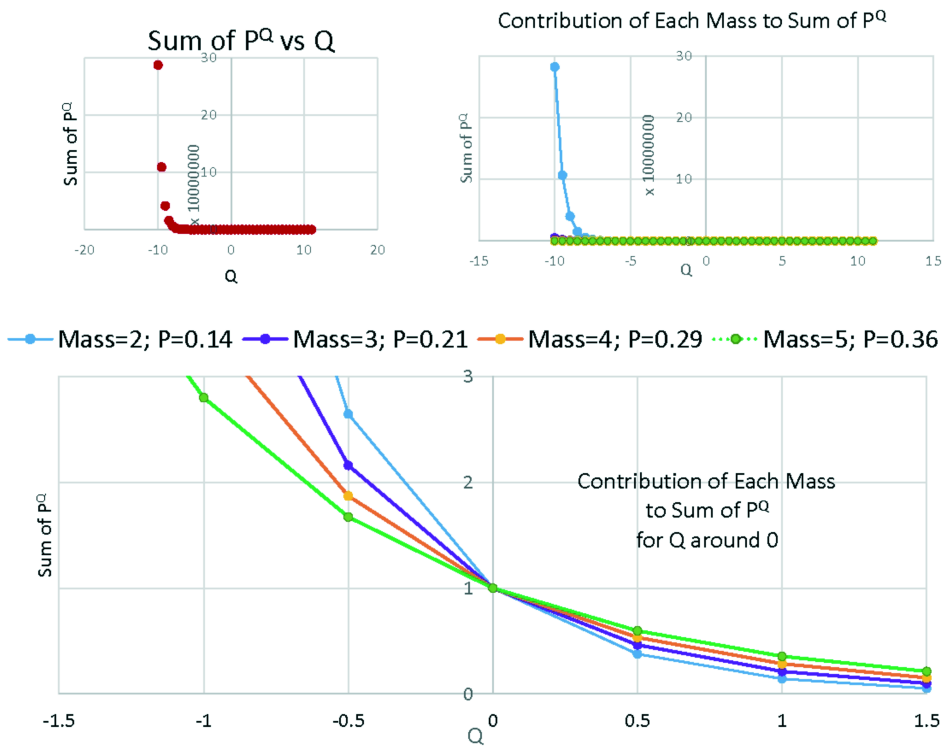

Fig. 4. *Relationships amongst P, Q and $I_{k(Q)}$.* The graphs are based on a hypothetical probability distribution, where the total number of boxes containing any mass at some box size was four. The four boxes had respective masses (Equation (10)) of 2, 3, 4, and 5, so that the total mass (Equation (11)) was their sum, 14. The probabilities (Equation (12)) thus were, for mass = 2, $P = 2/14 = 0.14$, for mass = 3, $P = 3/14 = 0.21$, for mass = 4, $P = 4/14 = 0.29$, and for mass = 5, $P = 5/14 = 0.36$, totaling 1.00. The vertical axes on the graphs represent the value of Equation (13), the sum of the four probabilities each raised to Q, over an arbitrary range of Qs. The top left shows the sum as the total of all four probabilities over the range of Qs, and the top right and bottom figures compare the contributions of each probability to that sum. The bottom figure expands the top right around $Q = 0$, showing that when Q is negative, the sum is amplified more by areas with smaller probabilities (e.g., see the contribution of the mass = 2 for $Q < 0$ on both figures), but this reverses at 0, so that when Q is positive, the sum is amplified more by the denser probabilities.

In our box-counting software, we implement it as follows. First, the mass distribution, the set of $m_{(i,k)}$ for a k, is gathered using box-counting (Equations (10) and (11)). It contains information about how the pixel mass is distributed at each level of resolution or box size, B_k, but we are interested in the variation in this mass distribution at a finer level. Thus, we start looking at measures based on the Q-th moments of its probability distribution, P (Equation (12)). Specifically, P is exaggerated by raising each $P_{(i,k)}$ to each exponent Q in an arbitrary set of Qs. Typically, the set of Q includes positive and

negative exponents bracketed around 0, so the distribution is twisted up and down as we examine it. Next, the pattern, thus distorted at each box, i, is condensed into a single value based on the Q-th power moment sum, $I_{k(Q)}$ for that Q and B_k (see Equation (13)). As illustrated in Figure 4, because each term of the sum is a probability (i.e., between 0 and 1), negative Qs amplify the sum, positive shrink it, and $Q = 1$ gives the original measure. Smaller probabilities increase the sum more drastically for negative Qs, whereas positive Qs reduce the sum [22, 49].

$$m_{(i,k)} \qquad \text{Mass of pixels at this box, } i\text{, and size, } \mathrm{B}_k \tag{10}$$

$$M_k = \sum_{i=1}^{N_k} m_{(i,k)} \qquad \text{Total mass of pixels at this } k \tag{11}$$

$$P_{(i,k)} = \frac{m_{(i,k)}}{M_k} \qquad \text{Probability at the } i\text{-th box for this } k. \tag{12}$$

$$I_{k(Q)} = \begin{cases} \displaystyle\sum_{i=1}^{N_k} P_{(i,k)}^{Q} & \text{if } Q \neq 0 \text{ and } Q \neq 1\text{, the summed probabilities at this } k\text{,} \\ & \text{each first distorted by } Q\text{,} \\ 1 & \text{if } Q = 1\text{, the sum of all undistorted probabilities is 1,} \\ N_k & \text{if } Q = 0\text{, the sum of all probabilities each raised to the} \\ & \text{exponent 0 is equal to the box count at this } k. \end{cases} \tag{13}$$

The process is done for each Q and B_k to generate a series of $I_{k(Q)}$. Then, in the usual manner of finding a D_F discussed earlier, how this series of distorted mass information scaled with B_k is distilled into a D_Q for each Q (Equation (14)). The resulting set of D_Qs is plotted against Q to generate a multifractal graph showing if the distortions made much of a difference to the original distribution. The set of D_Q vs. Q is generated using the conditions outlined in Equations (14) and (15). The numerator (see Equation (13)) in the top condition in Equation (14) is calculated as the negative slope of the log-log regression line, as is done in regular box-counting. For the exception where $Q = 1$, $D_{Q=1}$ is found from the negative slope of the regression line for the so-called *information function* (Equation (15)). This is necessary to avoid 0 values for both the numerator and denominator (see [12, 64]) [12, 22, 58, 64, 68].

$$D_Q = \begin{cases} \dfrac{-\lim\limits_{\mathrm{B}_k \to 0} \left[\frac{\ln I_{k(Q)}}{\ln \mathrm{B}_k}\right]}{(1-Q)} & \text{if } Q \neq 1 \text{ (see Equation (13))} \\ -\lim\limits_{\mathrm{B}_k \to 0} \left[\dfrac{\ln \mathrm{S}_k}{\ln \mathrm{B}_k}\right] & \text{if } Q = 1 \text{ (see Equation (15))} \end{cases} \tag{14}$$

$$\mathrm{S}_k = \sum_{i=1}^{N_k} P_{(i,k)} \ln P_{(i,k)} \qquad \text{the entropy or information function.} \tag{15}$$

2.2. $f_{(\alpha)}$ vs. α multifractal singularity spectrum. Along with the D_Q, we use another multifractal analysis spectrum, the $f_{(\alpha)}$ vs. α curve. The method for finding it, relatively uncomplicated and readily implementable in box-counting [50], is based on

the methods of Chhabra and Jensen [12, 64]. Equations (16) to (20) explain how it is implemented in our box-counting software [46]. In essence, similar to the D_Q calculations, the method examines the distorted i-th probability, but it compares it to the sum of the distorted probability distribution. This normalized measure of the distorted distribution (Equation (16)) is used to calculate mass components (Equations (17) and (18)) for the α dimensions for each value of B_k and Q (i.e., for computing the average singularity strength, α_i, with respect to $\mu_{i,k(Q)}$). For $Q > 0$, $\mu_{i,k(Q)}$ amplifies the more singular parts of the probability distribution. (See Figure 5.)

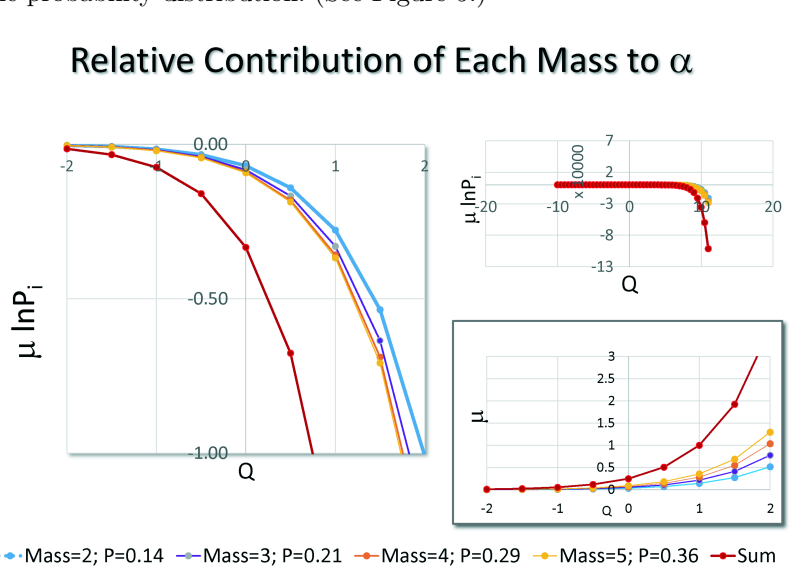

Fig. 5. *How Q affects α_i.* The vertical axes represent the mass components used for calculating α_i from Equation (19) for the hypothetical probability distribution for masses of 2, 3, 4, and 5 shown in the legend (explained in Figure 4). The left and top figures show how Q affects Equation (17) and the bottom figure how it affects Equation (16). All three show that higher values of Q amplify the sum more for more dense probabilities. For $Q = 1$, Equation (16) = the original probability. Compare to Figure 4.

Those values in turn are used to find slopes against B_k for the α dimensions at each Q (Equations (19) and (20)). The multifractal spectra are then obtained by examining how $f_{(\alpha)}$ is related to α for each Q by plotting $f_{(\alpha)}$ vs. α (Equation (19) horizontally and (20) vertically).

$$\mu_{i,k(Q)} = \frac{P_{(i,k)}^{Q}}{I_{k(Q)}} \qquad \begin{array}{c}\text{normalized measure of the probability}\\ \text{distribution (see Equations (13) \& (12))}\end{array} \tag{16}$$

$$\alpha_{k(Q)} = \sum_{i=1}^{N_k} [\mu_{i,k(Q)} \ln P_{(i,k)}] \qquad \text{mass component of } \alpha \text{ dimension at } \mathrm{B}_k \tag{17}$$

$$f_{(\alpha_{k(Q)})} = \sum_{i=1}^{N_k} [\mu_{i,k(Q)} \ln \mu_{i,k(Q)}] \qquad \text{mass component of } f_{(\alpha)} \text{ dimension at } \mathrm{B}_k \tag{18}$$

$$\alpha_{(Q)} = -\lim_{\mathrm{B}_k \to 0} \frac{\alpha_{k(Q)}}{\ln \mathrm{B}_k} \qquad \alpha \text{ dimension; as slope of regression line} \tag{19}$$

$$f_{(\alpha_{(Q)})} = -\lim_{\mathrm{B}_k \to 0} \frac{f_{(\alpha_{k(Q)})}}{\ln \mathrm{B}_k} \qquad f_{(\alpha)} \text{ dimension; as slope of regression line.} \tag{20}$$

This method also leads to an alternative method for calculating D_Q and another useful measure, τ. It can be seen from Equations (9) and (13) that $I_{k(Q)}$ varies as B_k to some exponent, τ_Q, so that

$$I_{k(Q)} = \mathrm{B}_k^{\tau_Q} \therefore \tau_Q = \log_{\mathrm{B}_k} I_{k(Q)} = \frac{\ln I_{k(Q)}}{\ln \mathrm{B}_k}. \tag{21}$$

Thus, τ_Q is equivalent to the numerator in Equation (14) so D_Q can be alternatively calculated from Equations (22) and (23) [12, 17, 40, 64]:

$$D_Q = \frac{\tau_Q}{Q-1} \tag{22}$$

$$\tau_Q = Q\alpha_{(Q)} - f_{(\alpha_{(Q)})} \qquad \text{see Equations (19) and (20).} \tag{23}$$

2.3. Interpreting multifractal spectra. Multifractal spectra convey easily observable information. Patterns that scale uniformly distort the probability distribution little, whereas those that scale non-uniformly yield distinct mathematical views for both the D_Q vs. Q and $f_{(\alpha)}$ vs. α multifractal spectra.

2.3.1. *D_Q vs. Q spectra.* Figure 6 shows D_Q vs. Q plots obtained by box-counting for three figures illustrating non-fractal, monofractal, and multifractal scaling. As the figure illustrates, the generalized dimension curve is usually either essentially unchanging or decreasing around $Q = 0$, with dimensional ordering such that $D_{Q=0} \geq D_{Q=1} \geq D_{Q=2}$. In practice, the D_Q vs. Q curve is typically fairly flat for non-fractals, less for monofractals (i.e., theoretically, $D_{Q=0} = D_{Q=1} = D_{Q=2}$ if a pattern is homogeneous and self-similar). For multifractals, it typically decreases with Q, sigmoidally around $Q = 0$. Also of note, $D_{Q=0}$ is the capacity dimension (see Equation (13)) equivalent to the D_B, $D_{Q=1}$ is the information dimension (see Equation (15)) where $D_Q = f_{(\alpha)} = \alpha$, and $D_{Q=2}$ is the correlation dimension [68, 85].

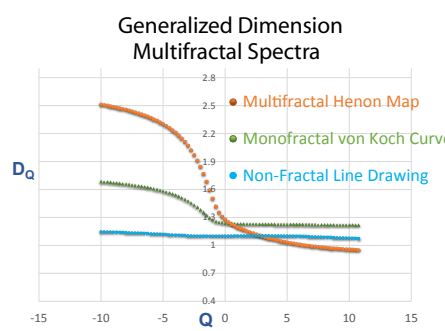

Fig. 6. *Typical multi-, mono-, and non-fractal D_Q vs. Q curves obtained by box-counting.* Theoretical D_F: Henon Map ≈ 1.27; von Koch Curve ≈ 1.26; Rectangle ≈ 1.00.

One way to quantify variation in the D_Q plot is using the coefficient of variation (CV), calculated as $\frac{\text{standard deviation}}{\text{mean}}$ in values for the regression line. The CV for the D_Q plot is generally greatest for multifractals, although the value is affected by methodological matters including image size [49].

2.3.2. $f_{(\alpha)}$ *vs.* α *spectra.* As illustrated in Figure 7, $f_{(\alpha)}$ vs. α curves typically rise to a maximum approximating the D_B and then fall, where in general greater variability in a pattern gives a broader spectrum. Non- and mono-fractals typically converge (especially for $Q > 0$, i.e., the left side), but multifractals rise and fall more broadly. The relative sharpness or *aperture* (Figure 8) and spread between maximum and minimum $\alpha_{(Q)}$ quantitate the degree of multifractality and distinguish multifractals from other patterns. The aperture is defined by the slope and length of the line segments from $\alpha_{(-1)}$ to $\alpha_{(0)}$ to $\alpha_{(1)}$ [64], [22, 49].

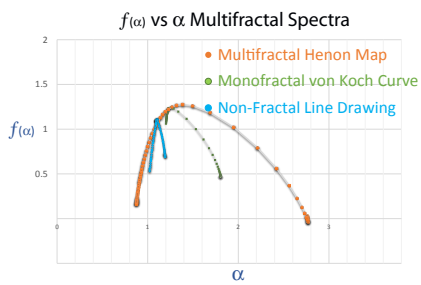

Fig. 7. *Typical multi-, mono-, and non-fractal* $f_{(\alpha)}$ *curves obtained by box-counting.* See Figure 6 for D_Fs.

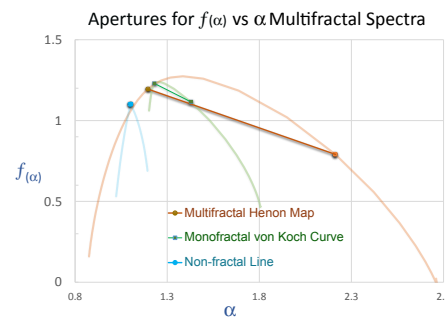

Fig. 8. *Apertures.* The aperture is the line from $\alpha_{(-1)}$ to $\alpha_{(0)}$ to $\alpha_{(1)}$. The extremely short aperture for the line drawing appears as a point.

2.3.3. *Practical limitations.* There are caveats to interpreting these curves. They can be profoundly affected by methodological issues such as image size and data processing, for instance. In addition, there is a deviation from the prototypical patterns and controversy about the threshold between fractal and multifractal. In this regard, some software (e.g., FracLac [46]), includes mechanisms for objectively quantifying features of the curves and determining the optimum from several samplings including rotations of the same image, and for filtering the data (e.g., smoothing or finding the minimum cover).

Furthermore, when applying multifractal spectral analysis, one must be aware that what we have described here is a *post hoc* analytical technique rather than a complete description of multifractal theory, which is a topic surrounded by much controversy [18, 33]. More detailed discussion of these considerations is beyond the scope of this paper, but overall, one must realize that an ostensibly multifractal result does not guarantee that a multifractal phenomenon governs the original from which the pattern was extracted for analysis. Nor does it tell what elements of a phenomenon are or are not multifractal. Rather, multifractal analysis gives a measure that can be very powerful when tested rigorously, including calibration with control images, and interpreted cautiously [23, 33, 34, 38].

3. Applying multifractal spectral analysis

3.1. Microglia. We have used multifractal analysis extensively in neuroscience research, a field where fractal analysis is developing rapidly [18]. Some of our recent work focuses on microglia. In brief, microglia are neuroimmune cells residing in the brain and spinal cord

in many species, including humans, playing key roles in not just pathology but also normal physiology and development [71, 82]. Their form reflects their function and therefore the general status of the brain and nervous system (see Figure 9). Our lab and others have used mono-fractal methods to objectively quantitate and classify microglial morphology and correlate decreasing D_Fs with increasing pathology, and have found that multifractal analysis complements these methods in a few key applications [5, 26, 35, 50, 76].

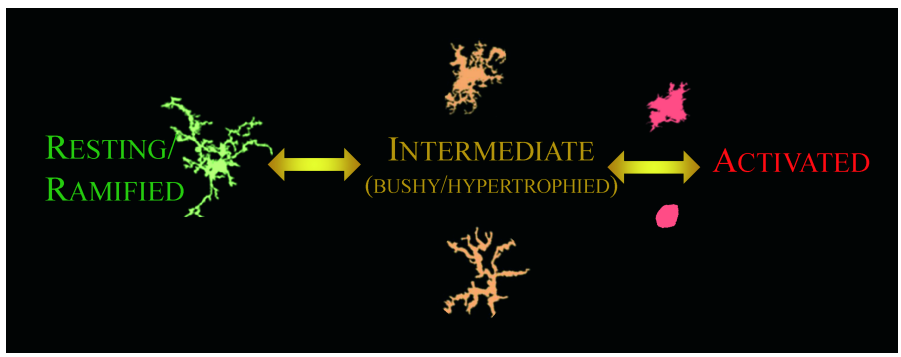

Fig. 9. *Complexity of Microglial Morphology.* Microglia cycle through a continuum of typical morphologies [50]. Ramified facilitate normal activity, staying alert for trauma, pathology, stress [26], etc. Intermediate are responding to events or returning to ramified. Activated aggressively mediate tissue breakdown and repair, act as macrophages, etc. The D_F is highest for ramified and lowest for activated [71]. Cells between ramified and intermediate are most amenable to multifractal analysis [38, 49, 47].

3.1.1. *Multifractal analysis for discerning transitional states.* Our lab has shown previously that the D_B distinguishes even very subtle differences that are not detectable visually, and can be used to objectively classify microglia, in particular by separating resting cells in pathological environments from resting cells in non-pathological environments [35, 50, 47]. As suggested in Figure 9, the general trend in microglia research indicates very strongly that individual microglial cells from overall healthier biological environments have higher fractal dimensions [26, 38, 76]. This is in keeping with the general notion that as physiologic systems fail they lose complexity, their information content degrades, and they become less and less able to adapt to a dynamic environment, respond in novel ways, or cope with emergencies [18, 55]. When we have looked at microglia under the lenses of multifractal analysis we have found that, overall, in various studies, about 10% of microglia show variation in the CV enough to be considered to show multifractal scaling, these being primarily ramified cells. We have also found a tendency for multifractal scaling to be found more in aging. A noteworthy strength of multifractal analysis is its ability to detect cells presumably in transition between ramified and intermediate stages. Moreover, amongst cells that show multifractal scaling, a "pseudomultifractal" pattern has been observed, whereby D_Q vs. Q slopes are flatter than usually seen, and $f_{(\alpha)}$ spectra more peaked and converging compared to benchmark multifractal spectra, but not clearly converging as with typical mono- and non-fractals [38, 47].

3.1.2. *In silico modeling and multifractal analysis.* We have found similar results investigating multifractal scaling in microglia using *in silico* modeling. One of our most

interesting findings sheds some light on the ability of multifractal analysis to identify transitional cells. Basically, these computer-based morphological simulation studies have shown that microglia modeled from a single set of branching parameters were less likely to scale as multifractals than were models made using multiple different sets, simulating disparate cell parts and activity similar to the activity, motion, and dynamic morphological changes seen in real microglia [36, 38, 49].

3.1.3. *Future applications of multifractal analysis to microglia.* A challenge that remains for the future is to pursue the potential for multifractal analysis to identify cells in transitional stages and to act as a supplement to the D_B for discovering subtle differences relevant to fields such as aging and chronic disease. Future work could also explore multifractal scaling over large tissue samples in addition to images of individual cells in order to understand broader dynamics. Another question to pursue is what the meaning and implications are of increasing multifractality in transitional stages. This could have very important implications for how we treat and diagnose disease of the central nervous system.

On another note, the studies reviewed here capture only specific points in time and space. Fractal analysis of microglia has chiefly so far used binary images of individual cells to capture scaling in the branching and edge features of whole cells, but microglia are very dynamic—they unfurl and wave their processes about in healthy tissue [59, 70, 81], for instance, and as cells change from resting, their fine processes retract, tendrils swell, and stouter ones extend in the course of a response to noxious stimuli [26]. Furthermore, these cells move and the space they occupy itself is dynamic [70, 82]. As such, another challenge for the future is to explore fractal and multifractal scaling over time in individual cells and over areas and volumes *in vivo* and *in vitro*. With the advent of new technologies allowing for real-time observation of live events at the cellular level, at least in laboratory animals, these challenges seem within reach [59].

3.2. Cervical intraepithelial neoplasia. Another area in which we have applied the techniques described here is cancer research. We have recently published work on cervical intraepithelial neoplasia (CIN), a significant health care burden around the globe [41, 42]. Early diagnosis is critical because cervical cancer is largely curable if caught before it degrades to invasive stages, yet grading depends on the expertise of individual pathologists since most methods in use are semi-quantitative and not objective. One of the current goals in this field is to develop new and practical approaches for objectively grading CIN and normal tissue [7].

A substantial body of evidence indicates that monofractal and multifractal methods are promising for classifying tumours using digital images [2, 3, 4, 29, 43, 84]. We have worked with digital images of biological tissue stained with a commonly used dye, haematoxylin and eosin (HE), obtained with a microscope and camera system. These are typical images that pathologists would use for grading CIN. We have found that D_Q vs. Q multifractal spectra from box-counting can be used to differentiate between normal epithelium and low grade as well as high grade neoplasia for cervical cancer [21].

As a measure of complexity, multifractal analysis is especially pertinent in cancer research because of not just changes in complexity of individual cells associated with

disease, but also broader differences in complexity over the tissue, as might be seen in a whole biological image (See Figure 10). Such complexity is presumably attributable to multiple processes acting on tissue over time and at different scales, both microscopic and macroscopic. Tissue that is organized into interacting parts where each has its own function would be expected to scale as a multifractal, whereas tissue that has lost this separation of function and begun to become a more homogeneous but dysfunctional mass would be more likely to scale as a monofractal. That is, finding the D_B of individual cells as we discussed for microglia is not the same as taking the multifractal spectra of the entire area those cells are in, but both kinds of analysis can inform us (See Figure 11.)

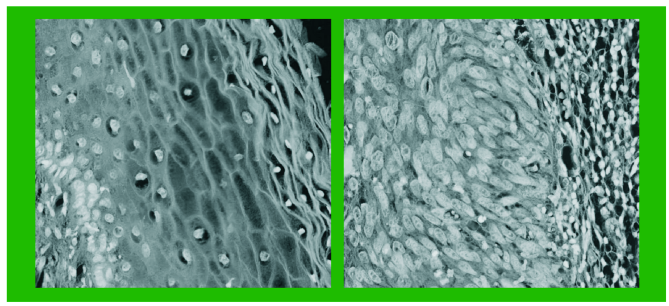

Fig. 10. *Grayscale images of HE stained tissue.* Left: Control tissue. Right: CIN3 tissue.

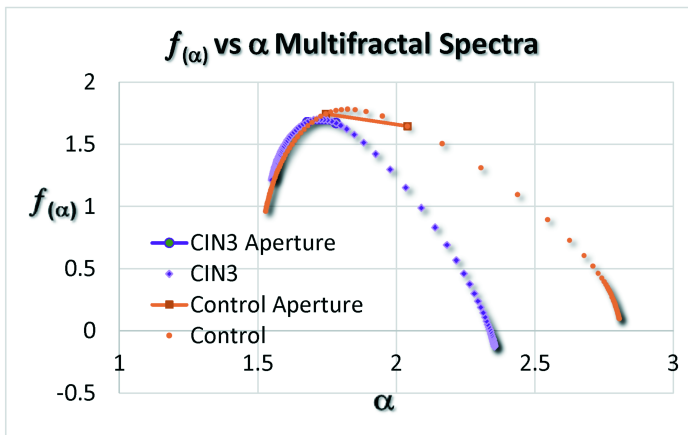

Fig. 11. *Examples of multifractal spectra for Grayscale CIN images.* Multifractal spectra for the example images shown in Figure 10.

3.2.1. *Gray-scale analysis.* Although the box-counting methodology we described here applied to binary images, in which a pixel is either background or non-background, grayscale images can also be assessed, such as when the "background" the cells of interest are embedded in is actually part of the signal to investigate. For multifractal analysis on gray-scale images using the basic box-counting technique, the key difference from binary images is that the information gathered at each i-th box of size B_k depends on the intensity, h, of the signal in the box. It is assumed that $h \propto height$, so h is used to infer a volume of significance as opposed to a mass or count. One way to describe the

volume is to let h be the difference between the maximum and minimum intensities of all pixels in a box, and multiply that height by the measure of the base sampling unit (i.e., a box for a cube or an oval for a cylinder) [46]. Figure 11 presents multifractal spectra for the unsegmented grayscale images from Figure 10, illustrating a loss in multifractality comparing normal to pathological (CIN3).

We anticipate using fractal and multifractal analysis to further develop our preliminary system for automated diagnosis of CIN. The ultimate goal is an easy, inexpensive, objective, and reliable method sensitive enough for automated image diagnosis from readily obtainable images such as those a pathologist currently views, incorporating individual cell features as well as more general tissue features. Another goal is for this software to yield a specific prognosis, such as by using fractal dimensions to predict if CIN 1 lesions are more likely to degrade to CIN 2 or to become normal again, and to further characterize changes within low grade neoplasia and specifically CIN 3 identified by multifractal spectra [21].

4. Other multifractal implementations. There are many techniques in addition to box-counting that use the multifractal formalism. Here we briefly introduce two examples, the correlation dimension and time series analysis, as applied to two clinically timely areas of research in biology and medicine.

4.1. Retinal pathology. Retinopathy is a progressive menace afflicting a high proportion of diabetics and often eventually leading to blindness [20, 25]. As with CIN, early diagnosis and intervention are critical to managing this enormous global health burden. One component of early diagnosis is automated classification of digital images into retinas with or without PR; this needs to be very accurate to support screening programs currently carried out by ophthalmologists. Developing objective, reliable, and practical methods of automating screening, especially for remote settings where specialists are not generally present but retinopathy is, continues to be a major goal in diabetes research [30, 39, 32, 63].

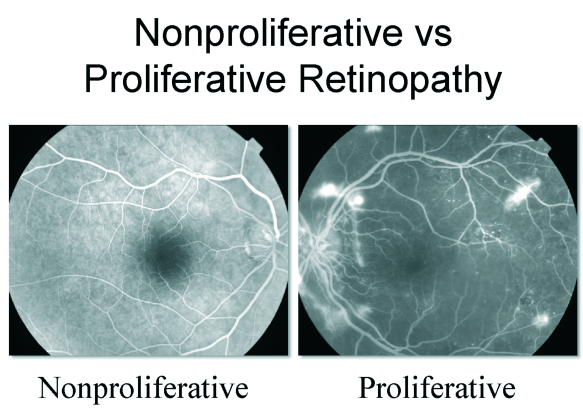

Fig. 12. Two stages of diabetic retinopathy.

4.1.1. *Classification.* Diabetic retinopathy can be considered in terms of two stages, nonproliferative (NPR) or proliferative (PR). These categories may be further graded by severity and the features of lesions present within each [20, 25]. Basically, in PR, new blood vessels emerge near the optic disk and spread toward the macula or emerge from peripheral vessels. These new vessels are abundant, but dysfunctional. Rather than resupplying a starving retina, they compound problems largely because they are both fragile and often misplaced [83, 88, 89]. Figure 12 illustrates two retinal images depicting some typical differences between NPR and PR.

4.1.2. *Correlation dimension.* Much research has demonstrated that PR is amenable to study by the many methods of fractal analysis [11, 16, 31, 39, 32, 48, 51, 52, 54, 61, 80]. Here we briefly discuss a special case of the multifractal formalism involving the correlation dimension, otherwise known as $D_{Q=2}$ (see Section 2.3.1), and apply it to automated classification of PR. According to multifractal theory, $D_{Q=2}$ measures the dimension of the space occupied by a set of random points, in terms of the probability of finding two points closer than a certain distance. For a digital image, it can be found using the method described earlier here based on the Q-th order moment of a distribution to find the probability $P_{(i,k)}$ of finding a point in the i-th box (see Section 2.1). The probability of finding two points at i corresponds to $Q = 2$, i.e., $P^2_{(i,k)}$. Equation (14) tells us that the correlation dimension, $D_{Q=2}$, can be calculated:

$$D_{Q=2} = \frac{-\lim_{\mathrm{B}_k \to 0}\left[\frac{\ln I_{k(2)}}{\ln \mathrm{B}_k}\right]}{-1} = \lim_{\mathrm{B}_k \to 0}\left[\frac{\ln I_{k(2)}}{\ln \mathrm{B}_k}\right] \tag{24}$$

$$I_{k(2)} = \sum_{i=1}^{N_k} P^2_{(i,k)}. \tag{25}$$

Equation (25) can be thought of as essentially the probability of having a pair of points less than B_k apart, although strictly speaking, that would only hold for circles because, for instance, two points at opposite corners of a square will be farther apart than the size of the side of the box. An often used mathematical description, based on the *correlation sum* or *correlation integral* (C_{B_k}), is outlined below, showing how the correlation dimension can be calculated from the C_{B_k} using the distances between each pair of points in a set of N points [9, 22, 64].

$$M \qquad \text{number of points } i \text{ in the set}$$

$$\eta = \frac{M^2 - M}{2} \qquad \text{number of pairs of points } i, j > i \text{ in the set} \tag{26}$$

$$\Delta_{i,j} = \left|X_i - X_j\right| \qquad \text{distance between points } i \text{ and } j \tag{27}$$

$$\mathrm{B}_k \qquad \text{scaling distance at this iteration, } k$$

$$W_{\mathrm{B}_k} = \sum_{i=1, j>i}^{M} H_{i,j} \qquad \text{number of pairs where } \Delta_{i,j} \leq \mathrm{B}_k \tag{28}$$

$$H_{i,j} = \theta(\mathrm{B}_k - \Delta_{i,j}) = \begin{cases} 1 & \text{if } \Delta_{i,j} \le \mathrm{B}_k \\ 0 & \text{otherwise} \end{cases} \quad \text{function counts pairs within scaling distance} \tag{29}$$

$$C_{\mathrm{B}_k} = \lim_{M\to\infty} \frac{W_{\mathrm{B}_k}}{\eta} \quad \text{probability of pairs within scaling distance} \tag{30}$$

$$C_{\mathrm{B}_k} \propto A\mathrm{B}_k^{D_{Q=2}} \tag{31}$$

$$D_{Q=2} = \lim_{\mathrm{B}_k\to 0}\Big[\frac{\ln C_{\mathrm{B}_k}}{\ln \mathrm{B}_k}\Big]. \tag{32}$$

The correlation dimension has been an important part of our work developing automated diagnosis systems for PR. We have applied it to develop a system for automatic segmentation of digital images of the retina, then to further classify the images as PR or not. On its own, the correlation dimension had some predictive ability, but when it was used in a set of six best features (area, perimeter, entropy, curvature, median correlation dimension, and global correlation dimension), the results were very promising. In particular, the set had an AUC of 0.90 (0.73–0.97). (AUC stands for "area under the curve" and is a way of measuring the likelihood of a test giving "true positive" as opposed to "false positive" results. 0.90 means, basically, a 90% chance of a true positive) [31].

5. Multifractal time series analysis

5.1. Heart rate variability. Whereas this discussion has focused on digital image analysis, the fundamental concepts of multifractal analysis also apply to time series analysis, such as heart rate variability (HRV) analysis [14, 44]. Cardiac cycles are not constant; they show clear multifractal scaling. In the healthiest hearts, they vary on extremely short and long time scales involving cascading and coupled feedback loops, where the loss of variability, a degradation of multifractality to monofractality in particular, is predictive of pathology (e.g., congestive heart failure, fetal acidosis) and generally understood to be a loss of the ability to respond to changes in the environment [1, 28]. Here we discuss some applications of multifractal analysis to cardiac autonomic neuropathy (CAN), which, in brief, means nerve damage leading to abnormal control of heart rate that often leads to arrhythmia and heart attack. The disease is a severe global health burden, affecting diabetics in particular [30, 44, 60]. Detection of CAN relies on invasive and time- and labour-consuming methods, such that many people at risk are not routinely screened. As with CIN and PR, early detection of CAN is key to disease management, so automatic detection from a simple measure such as HRV is a major research goal.

Usually, HRV is measured from electrocardiograph (ECG) signal. Work is also being done on more portable technology such as pulse waves acquired from a small, easily worn light source and photo detector [66], but currently ECG is standardly used for gauging HRV. Certain peaks in the ECG signal, the tall R peaks, are well suited to automated computer detection, so the distance between peaks, called the RR interval, generally form the basis of the time series usually studied in HRV analysis [15].

There are many systems for measuring HRV using the RR interval, including many different ways of doing multifractal analysis on HRV RR data (see [86] for a review). Here we provide a simple overview to highlight a few key principles of one general type of multifractal HRV analysis. As was the case with the other types of multifractal analysis discussed here, in HRV analysis, there is always the question of how to extract a pattern from the original signal. Typically, this involves some amount of filtering to remove noise and ectopic beats, for instance, to generate a pre-processed signal. To apply a multifractal analysis, the usually pre-processed signal has to be read as a probability distribution that catches the presumed multifractal features. One multifractal measure that has been applied is Multi-lag Tone-Entropy, which has been shown to identify increased risk of cardiac mortality in people with diabetes [44]. In the Tone-Entropy (TE) method, the signal is converted to *tone* and *entropy* components based on a measure of interbeat characteristics called the percentile index (PI). For an RR interval, PI scales the change between beats against the first beat in the interval, modeling the system as interactive increases and decreases in heart rate. In Multi-lag TE, the lag L can vary, as in Equation (33) [37, 44].

$$PI = \frac{R_i - R_{i+L}}{R_i}(100). \tag{33}$$

Tone is then calculated as the average of the PI series, so that it represents a net balance between increases and decreases for a particular lag:

$$Tone = \frac{\sum_{i=1}^{N-1} PI_i}{N-1} \qquad N-1 \text{ denotes that the last PI cannot be determined.} \tag{34}$$

Then, a probability distribution (see [44] for details), P, for *Tone* is determined and used to calculate entropy using some form of the basic Entropy function we saw in Equation (15):

$$I = \sum_{i=1}^{N} [P_i \log (P_i)]. \tag{35}$$

A similar measure, *Multi Scale Renyi Entropy*, has been demonstrated in research to be able to distinguish CAN from controls even in the early stages of the disease [14]. In this method, basically, the Renyi entropy is calculated from the probability of sequences of RR values occurring in HRV data. This probability is estimated by its similarity with all other sequences of the same length, and entropy is calculated for a range of exponents, α:

$$I_\alpha = \frac{\sum_{i=1}^{N_k} {P_i}^\alpha}{1-\alpha}\,. \tag{36}$$

These examples of how multifractal analysis can be applied to HRV are important, because they offer clear hope that simple and relatively non-invasive tests for early CAN will soon be available, along with all the benefits that implies for improving the quality of life of people living with this disease [1, 14].

6. Conclusion. Many physiologic systems are inherently multifractal, self-seeding, cascading, interacting with themselves and the environment in multifarious ways but when degraded to pathological states are less complex, structurally and functionally, including being less adaptable to the constantly changing environment, being unable to behave in novel ways, becoming dangerously predictable. In many cases, it is known that early intervention is critical to avoiding permanent damage, a crisis, or death. Multifractal analysis sits at the cusp of a wave of technological change preparing to identify and address many of these vexing problems in biology and medicine.

References

[1] P. Abry, H. Wendt, S. Jaffard et al., *Methodology for multifractal analysis of heart rate variability: from LF/HF ratio to wavelet leaders*, in: Engineering in Medicine and Biology Society (EMBC), 2010 Annual International Conference of the IEEE, 106–109.

[2] R. Abu Eid, G. Landini, *Quantification of the global and local complexity of the epithelial-connective tissue interface of normal, dysplastic, and neoplastic oral mucosae using digital imaging*, Pathol. Res. Pract. 199 (2003), 475–482.

[3] H. Ahammer, T. T. DeVaney, H. A. Tritthart, *Fractal dimension of* K1735 *mouse melanoma clones and spheroid invasion in vitro*, Eur. Biophys. J. 30 (2001), 494–499.

[4] H. Ahammer, J. Kroepfl, C. Hackl, R. Sedivy, *Fractal dimension and image statistics of anal intraepithelial neoplasia*, Chaos Solitons Fractals 44 (2011), 86–92.

[5] J. Andjelkovic, N. Zivic, B. Reljin, V. Celebic, I. Salom, *Application of multifractal analysis on medical images*, WSEAS Transactions on Information Science & Applications 5 (2008), 1561–1572.

[6] A. B. Ariza-Villaverde, F. J. Jiménez-Hornero, E. Gutiérrez De Ravé, *Influence of urban morphology on total noise pollution: multifractal description*, Science of the Total Environment 472 (2014), 1–8.

[7] A. H. Beck, A. R. Sangoi, S. Leung et al., *Systematic analysis of breast cancer morphology uncovers stromal features associated with survival*, Science Translational Medicine 3 (2011), art. 108ra113.

[8] O. Binah, A. Weissman, J. Itskovitz-Eldor, M. R. Rosen, *Integrating beat rate variability: from single cells to hearts*, Heart Rhythm 10 (2013), 928–932.

[9] M. Y. Boon, B. I. Henry, C. M. Suttle, S. J. Dain, *The correlation dimension: A useful objective measure of the transient visual evoked potential?*, Journal of Vision 8 (2008), art. 6.

[10] Y. Chen, J. Wang, *Multifractal characterization of urban form and growth: the case of Beijing*, Environment and Planning B: Planning and Design 40 (2013), 884–904.

[11] C. Y. Cheung, G. N. Thomas, W. Tay et al., *Retinal vascular fractal dimension and its relationship with cardiovascular and ocular risk factors*, Amer. J. Ophthalmol. 154 (2012), 663–674.

[12] A. Chhabra, R. V. Jensen, *Direct determination of the $f(\alpha)$ singularity spectrum*, Phys. Rev. Lett. 62 (1989), 1327–1330.

[13] D. Cornforth, H. Jelinek, L. Peichl, *Fractop: a tool for automated biological image classification*, in: Proceedings of the Sixth AI Australasia-JapanWorkshop, Citeseer, 2002, 141–148.

[14] D. J. Cornforth, M. P. Tarvainen, H. F. Jelinek, *Using Renyi entropy to detect early cardiac autonomic neuropathy*, in: Engineering in Medicine and Biology Society (EMBC), 2013 35th Annual International Conference of the IEEE, 2013, 5562–5565.

[15] D. J. Cornforth, M. P. Tarvainen, H. F. Jelinek, *How to calculate Renyi entropy from heart rate variability, and why it matters for detecting cardiac autonomic neuropathy*, Frontiers in Bioengineering and Biotechnology 2 (2014), art. 34.

[16] M. J. Cree, H. F. Jelinek, *Image analysis of retinal images*, in: Medical Image Processing, Springer, New York 2011, 249–268.

[17] S. De Bartolo, S. Gabriele, R. Gaudio, *Multifractal behaviour of river networks*, Hydrology and Earth System Sciences Discussions 4 (2000), 105–112.

[18] A. Di Ieva, F. Grizzi, H. Jelinek, A. J. Pellionisz, G. A. Losa, *Fractals in the neurosciences. Part I. General principles and basic neurosciences*, The Neuroscientist 20 (2014), 403–417.

[19] S. Dutta, D. Ghosh, S. Chatterjee, *Multifractal detrended fluctuation analysis of human gait diseases*, Front. Physiol. 4 (2013), art. 274.

[20] ETDRS, *Grading diabetic retinopathy from stereoscopic color fundus photographs–an extension of the modified Airlie House classification*, ETDRS (Early Treatment Diabetic Retinopathy Study Research Group) Report No. 10, Ophthalmology 98 (1991), 786–806.

[21] M. Fabrizii, F. Moinfar, H. F. Jelinek, A. Karperien, H. Ahammer, *Fractal analysis of cervical intraepithelial neoplasia*, PLoS One 9 (2014), art. e108457.

[22] K. Falconer, *Fractal Geometry: Mathematical Foundations and Applications*, 3rd ed., Wiley, Chichester 2014.

[23] E. Fernández, J. A. Bolea, G. Ortega, E. Louis, *Are neurons multifractals?*, J. Neuroscience Methods 89 (1999), 151–157.

[24] J. Goñi, O. Sporns, H. Cheng et al., *Robust estimation of fractal measures for characterizing the structural complexity of the human brain: Optimization and reproducibility*, NeuroImage 83 (2013), 646–657.

[25] N. Health, M. R. Council, *National evidence based guidelines for the management of type 2 diabetes mellitus*, Australian Centre for Diabetes Strategies, 2001.

[26] M. Hinwood, R. J. Tynan, J. L. Charnley, S. B. Beynon, T. A. Day, F. R. Walker, *Chronic stress induced remodeling of the prefrontal cortex: structural re-organization of microglia and the inhibitory effect of minocycline*, Cerebral Cortex 23 (2013), 1784–1797.

[27] P. M. Iannaccone, M. Khokha, *Fractal Geometry in Biological Systems: an Analytical Approach*, CRC Press, New York 1996.

[28] P. C. Ivanov, L. A. Nunes Amaral, A. L. Goldberger et al., *Multifractality in human heartbeat dynamics*, Nature 399 (1999), 461–465.

[29] H. F. Jelinek, H. Ahammer, S. Matthews, P. Succar, C. S. McLachlan, M. Buckland, *Establishing a reference range for oligondendroglioma classification using Higuchi dimension analysis*, Biomedical Engineering / 765: Telehealth / 766: Assistive Technologies, 2012.

[30] H. F. Jelinek, D. Cornforth, *Fractal analysis in clinical screening and investigation*, in: Classification and Application of Fractals: New Research, Nova Science Publ., New York 2012, 277–301.

[31] H. F. Jelinek, M. J. Cree, J. J. G. Leandro, J. V. B. Soares, R. M. Cesar Jr, A. Luckie, *Automated segmentation of retinal blood vessels and identification of proliferative diabetic retinopathy*, J. Opt. Soc. Amer. A 24 (2007), 1448–1456.

[32] H. J. Jelinek, M. J. Cree, D. Worsley, A. Luckie, P. Nixon, *An automated microaneurysm detector as a tool for identification of diabetic retinopathy in rural optometric practice*, Clinical and Experimental Optometry 89 (2006), 299–305.

[33] H. Jelinek, N. Elston, B. Zietsch, *Fractal analysis: pitfalls and revelations in neuroscience*, in: Fractals in Biology and Medicine, Springer, 2005, 85–94.

[34] H. F. Jelinek, E. Fernandez, *Neurons and fractals: how reliable and useful are calculations of fractal dimensions?*, J. Neurosci. Methods 81 (1998), 9–18.

[35] H. Jelinek, A. Karperien, A. Buchan, T. Bossomaier, *Differentiating grades of microglia activation with fractal analysis*, Complexity International 12 (2008).

[36] H. Jelinek, A. Karperien, D. Cornforth, R. Cesar, J. Leandro, *Micromod: an l-systems approach to neuron modelling*, in: Proceedings of the Sixth Australasia-Japan Joint Workshop on Intelligent and Evolutionary Systems, Australian National Univ., Canberra 2002, 156–163.

[37] H. F. Jelinek, H. Md Imam, H. Al-Aubaidy, A. H. Khandoker, *Association of cardiovascular risk using non-linear heart rate variability measures with the Framingham risk score in a rural population*, Front. Physiol. 4 (2013), art. 186.

[38] H. F. Jelinek, N. T. Milošević, A. Karperien, B. Krstonošić, *Box-counting and multifractal analysis in neuronal and glial classification*, in: Advances in Intelligent Control Systems and Computer Science, Springer, New York 2013, 177–189.

[39] H. F. Jelinek, A. Rocha, T. Carvalho, S. Goldenstein, J. Wainer, *Machine learning and pattern classification in identification of indigenous retinal pathology*, in: Engineering in Medicine and Biology Society (EMBC), 2011 Annual International Conference of the IEEE, 5951–5954.

[40] F. Jestczemski, M. Sernetz, *Multifractal approach to inhomogeneous fractals*, Physica A 223 (1996), 275–282.

[41] J. Jordan, M. Arbyn, P. Martin-Hirsch et al., *European guidelines for quality assurance in cervical cancer screening: recommendations for clinical management of abnormal cervical cytology, Part 1*, Cytopathology 19 (2008), 342–354.

[42] J. Jordan, P. Martin-Hirsch, M. Arbyn et al., *European guidelines for clinical management of abnormal cervical cytology, Part* 2, Cytopathology 20 (2009), 5–16.

[43] Y. Kam, A. Karperien, B. Weidow, L. Estrada, A. R. Anderson, V. Quaranta, *Nest expansion assay: a cancer systems biology approach to in vitro invasion measurements*, BMC Res. Notes 2 (2009), 130–130.

[44] C. Karmakar, H. Jelinek, A. Khandoker et al., *Identifying increased risk of post-infarct people with diabetes using multi-lag Tone-Entropy analysis*, in: Engineering in Medicine and Biology Society (EMBC), 2012 Annual International Conference of the IEEE, 25–28.

[45] A. Karperien, *FracLac for ImageJ: Javadoc, source code, and jar*, 2001.

[46] A. Karperien, *FracLac for ImageJ*, Charles Sturt Univ., 2013.

[47] A. Karperien, H. Ahammer, H. F. Jelinek, *Quantitating the subtleties of microglial morphology with fractal analysis*, Frontiers in Cellular Neuroscience 7 (2013), art. 3.

[48] A. Karperien, H. F. Jelinek, J. J. G. Leandro, J. V. B. Soares, R. M. Cesar Jr, A. Luckie, *Automated detection of proliferative retinopathy in clinical practice*, Clin. Ophthalmol. 2 (2008), 109–122.

[49] A. Karperien, H. Jelinek, N. Milošević, *Multifractals: a review with an application in neuroscience*, in: Proceedings of the 18th International Conference on Control Systems and Computer Science: Interdisciplinary Approaches to Fractal Analysis, Fifth Symposium on Interdisciplinary Approaches in Fractal Analysis, vol. 1, 2011, 888–893.

[50] A. Karperien, H. Jelinek, N. Milošević, *Reviewing lacunarity analysis and classification of microglia in neuroscience*, in: Fractals and Complexity, ed. P. Waliszewski, FA Format, Wrocław 2013, ISBN 978-83-936598-0-7, 50–56.

[51] G. Landini, G. P. Misson, P. I. Murray, *Fractal analysis of the normal human retinal fluorescein angiogram*, Current Eye Research 12 (1993), 23–27.

[52] G. Landini, P. I. Murray, G. P. Misson, *Local connected fractal dimensions and lacunarity analyses of 60 degrees fluorescein angiograms*, Investigative Ophthalmology & Visual Science 36 (1995), 2749–2755.

[53] J. Li, M. Ostoja-Starzewski, *Saturn's rings are fractal*, arXiv: 1207.0155.

[54] G. Liew, P. Mitchell, E. Rochtchina et al., *Fractal analysis of retinal microvasculature and coronary heart disease mortality*, Eur. Heart J. 32 (2011), 422–429.

[55] G. A. Losa, *Fractals in biology and medicine*, Encyclopedia of Molecular Cell Biology and Molecular Medicine, Wiley, 2011.

[56] B. B. Mandelbrot, *The Fractal Geometry of Nature*, vol. 173, Macmillan, 1983.

[57] B. B. Mandelbrot, *Negative fractal dimensions and multifractals*, Physica A 163 (1990), 306–315.

[58] B. B. Mandelbrot, C. J. G. Evertsz, Y. Hayakawa, *Exactly self-similar left-sided multifractal measures*, Phys. Rev. A (3) 42 (1990), 4528–4536.

[59] D. F. Marker, M.-E. Tremblay, S.-M. Lu, A. K. Majewska, H. A. Gelbard, *A thin-skull window technique for chronic two-photon in vivo imaging of murine microglia in models of neuroinflammation*, J. Vis. Exp. 43 (2010), art. e2059.

[60] R. E. Maser, B. D. Mitchell, A. I. Vinik, R. Freeman, *The association between cardiovascular autonomic neuropathy and mortality in individuals with diabetes: A metaanalysis*, Diabetes Care 26 (2003), 1895–1901.

[61] N. T. Milošević, M. Olujić, A. Oros, H. F. Jelinek, *Retinopathy of prematurity: Fractal analysis of images in different stages of the disease*, in: Advances in Intelligent Control Systems and Computer Science, Springer, New York 2013, 91–101.

[62] P. A. Moreno, P. E. Vélez, E. Martínez et al., *The human genome: a multifractal analysis*, BMC Genomics 12 (2011), art. 506.

[63] R. Pires, H. Jelinek, J. Wainer, S. Goldenstein, E. Valle, A. Rocha, *Assessing the need for referral in automatic diabetic retinopathy detection*, IEEE Transactions on Biomedical Engineering 60 (2013), 3391–3398.

[64] A. N. D. Posadas, D. Gimenez, M. Bittelli, C. M. P. Vaz, M. Flury, *Multifractal characterization of soil particle-size distributions*, Soil Science Society of America J. 65 (2001), 1361–1367.

[65] N. Sánchez, E. J. Alfaro, *The fractal spatial distribution of stars in open clusters and stellar associations*, in: Lecture Notes and Essays in Astrophysics IV, Torculo Press, Vigo 2010, 1–11.

[66] A. Schäfer, J. Vagedes, *How accurate is pulse rate variability as an estimate of heart rate variability? A review on studies comparing photoplethysmographic technology with an electrocardiogram*, Int. J. Cardiol. 166 (2013), 15–29.

[67] C. A. Schneider, W. S. Rasband, K. W. Eliceiri, *NIH Image to ImageJ: 25 years of image analysis*, Nature Methods 9 (2012), 671–675.

[68] M. R. Schroeder, *Fractals, Chaos, Power Laws: Minutes from an Infinite Paradise*, W. H. Freeman, New York 1991.

[69] K. G. Sheets, B. Jun, Y. Zhou et al., *Microglial ramification and redistribution concomitant with the attenuation of choroidal neovascularization by neuroprotectin* D1, Molecular Vision 19 (2013), 1747–1759.

[70] A. Sierra, S. Beccari, I. Diaz-Aparicio, J. M. Encinas, S. Comeau, M.-È. Tremblay, *Surveillance, phagocytosis, and inflammation: how never-resting microglia influence adult hippocampal neurogenesis*, Neural Plasticity 2014 (2014), art. 610343.

[71] A. Sierra, M.-È. Tremblay, H. Wake, *Never-resting microglia: physiological roles in the healthy brain and pathological implications*, Frontiers in Cellular Neuroscience 8 (2014), art. 240.

[72] S. Sleutel, V. Cnudde, B. Masschaele et al., *Comparison of different nano- and micro-focus X-ray computed tomography set-ups for the visualization of the soil microstructure and soil organic matter*, Computers & Geosciences 34 (2008), 931–938.

[73] V. B. Slezin, E. A. Korsakova, M. A. Dytjatkovsky, E. A. Schultz, T. A. Arystova, J. R. Siivola, *Multifractal analysis as an aid in the diagnostics of mental disorders*, Nordic J. Psychiatry 61 (2007), 339–342.

[74] T. Smith Jr, G. D. Lange, W. B. Marks, *Fractal methods and results in cellular morphology — dimensions, lacunarity and multifractals*, J. Neurosci. Methods 69 (1996), 123–136.

[75] T. Smith Jr, W. B. Marks, G. D. Lange, W. Sheriff Jr, E. A. Neale, *A fractal analysis of cell images*, J. Neurosci. Methods 27 (1989), 173–180.

[76] Z. Sołtys, M. Ziaja, R. Pawliński, Z. Setkowicz, K. Janeczko, *Morphology of reactive microglia in the injured cerebral cortex. Fractal analysis and complementary quantitative methods*, J. Neurosci. Res. 63 (2001), 90–97.

[77] C. Stan, C. Astefanoaei, E. Pretegiani et al., *Nonlinear analysis of saccade speed fluctuations during combined action and perception tasks*, J. Neurosci. Methods 232 (2014), 102–109.

[78] C. Stan, M. T. Cristescu, L. B. Iarinca, C. P. Cristescu, *Investigation on series of length of coding and non-coding DNA sequences of bacteria using multifractal detrended cross-correlation analysis*, J. Theoret. Biol. 321 (2013), 54–62.

[79] D. G. Stephen, J. R. Anastas, J. A. Dixon, *Scaling in executive control reflects multiplicative multifractal cascade dynamics*, Front. Physiol. 3 (2012), art. 102.

[80] T. Stosić, B. D. Stosić, *Multifractal analysis of human retinal vessels*, IEEE Transactions on Medical Imaging 25 (2006), 1101–1107.

[81] M.-È. Tremblay, R. L. Lowery, A. K. Majewska, *Microglial interactions with synapses are modulated by visual experience*, PLoS Biol. 8 (2010), art. e1000527.

[82] M.-È. Tremblay, B. Stevens, A. Sierra, H. Wake, A. Bessis, A. Nimmerjahn, *The role of microglia in the healthy brain*, J. Neurosci. 31 (2011), 16064–16069.

[83] S. Tremblay, K. Miloudi, S. Chaychi et al., *Systemic inflammation perturbs developmental retinal angiogenesis and neuroretinal function*, Investigative Ophthalmology & Visual Science 54 (2013), 8125–8139.

[84] J. Vasiljevic, B. Reljin, J. Sopta, V. Mijucic, G. Tulic, I. Reljin, *Application of multifractal analysis on microscopic images in the classification of metastatic bone disease*, Biomedical Microdevices 14 (2012), 541–548.

[85] T. Vicsek, *Fractal Growth Phenomena*, second ed., World Scientific, River Edge 1992.

[86] A. Voss, S. Schulz, R. Schroeder, M. Baumert, P. Caminal, *Methods derived from nonlinear dynamics for analysing heart rate variability*, Philos. Trans. R. Soc. Lond. Ser. A Math. Phys. Eng. Sci. 367 (2009), 277–296.

[87] Y. Xu, C. Qian, L. Pan, B. Wang, C. Lou, *Comparing monofractal and multifractal analysis of corrosion damage evolution in reinforcing bars*, PLoS One 7 (2012), art. e29956.

[88] J. C. S. Yam, A. K. H. Kwok, *Update on the treatment of diabetic retinopathy*, Hong Kong Med. J. 13 (2007), 46–60.

[89] J. W. Y. Yau, R. Kawasaki, F. M. A. Islam et al., *Retinal fractal dimension is increased in persons with diabetes but not impaired glucose metabolism: the Australian Diabetes, Obesity and Lifestyle* (*AusDiab*) *study*, Diabetologia 53 (2010), 2042–2045.